Article publicat / *Published paper*:

Trias, F.X, Gorobets, A., Oliva, A., Pérez-Segarra, C.D. DNS and regularization modeling of a turbulent differentially heated cavity of aspect ratio 5 (2013). *International Journal of Heat and Mass Transfer*, 57(1): 171-182. DOI: 10.1016/j.ijheatmasstransfer.2012.09.064

DNS and regularization modeling of a turbulent differentially heated cavity of aspect ratio 5

F. X. Trias[a], A. Gorobets[a], A. Oliva[a,*], C.D. Pérez-Segarra[a]

[a] *Heat and Mass Transfer Technological Centre (CTTC)*
Technical University of Catalonia (UPC)
C. Colom 11, 08222 Terrassa (Barcelona), Spain

Abstract

This work is devoted to the study of turbulent natural convection flows in differentially heated cavities. The adopted configuration corresponds to an air-filled ($Pr = 0.7$) cavity of aspect ratio 5 and Rayleigh number $Ra = 4.5 \times 10^{10}$ (based on the cavity height). Firstly, a complete direct numerical simulation (DNS) has been performed. Then, the DNS results have been used as reference solution to assess the performance of symmetry-preserving regularization as a simulation shortcut: a novel class of regularization that restrain the convective production of small scales of motion in an unconditionally stable manner. In this way, the new set of equations is dynamically less complex than the original Navier-Stokes equations, and therefore more amenable to be numerically solved. Direct comparison with the DNS results shows fairly good agreement even for very coarse grids.

Keywords: Differentially heated cavity, natural convection, turbulence, DNS, regularization modeling, symmetry-preserving

*Corresponding author
Email addresses: xavi@cttc.upc.edu (F. X. Trias), andrey@cttc.upc.edu (A. Gorobets), oliva@cttc.upc.edu (A. Oliva), segarra@cttc.upc.edu (C.D. Pérez-Segarra)

Nomenclature

A_1, A_3	depth and height aspect ratios, L_1/L_2 and L_3/L_2
C	dimensionless stratification, $\partial \langle\theta\rangle / \partial x_3 \vert_{\{x_2=\frac{1}{2A_3}, x_3=1/2\}}$
$\mathbf{C}(\mathbf{u}_h)$	discrete convective operator
$\mathbf{D}$	discrete diffusive operator
$\mathbf{f}$	dimensionless body force
$\mathbf{F}$	discrete filter, $\overline{\mathbf{u}_h} = \mathbf{F}\mathbf{u}_h$
g	gravitational acceleration
$\mathbf{L}$	discrete Laplacian operator, $-\mathbf{M}\mathbf{\Omega}^{-1}\mathbf{M}^t$
L_1, L_2, L_3	cavity depth, width and height
L_{ref}	reference length, L_3
$\mathbf{M}$	discrete divergence operator
N	dimensionless Brunt-Väisälä frequency, $(CPr)^{0.5}/(2\pi)$
$Nu(x_3)$	Nusselt number distribution at the hot wall, $-\partial \langle\theta\rangle / \partial x_2 \vert_{x_2=0}$
Nu	Nusselt number, $\int_0^1 Nu(x_3)dx_3$
$Nu_c(t)$	Nusselt number through the vertical mid-plane, $\int_0^1 (u_2\theta - \partial\theta/\partial x_2)\vert_{x_2=\frac{1}{2A_3}} dx_3$
N_1, N_2, N_3	number of nodes in the x_i-direction
p	dimensionless dynamic pressure
p_{ref}	reference dynamic pressure, $\rho\left(\alpha^2/L_3^2\right) Ra$
Pr	Prandtl number, ν/α
Ra	Rayleigh number based on cavity height, $(g\beta\Delta T L_3^3)/(\nu\alpha)$
$R_{\phi\phi}(x_1, x_2, r_3)$	two-point correlation, $\langle\phi'(x_1,x_2,x_3)\phi'(x_1,x_2,x_3+r_3)\rangle / \left\langle(\phi'(x_1,x_2,x_3))^2\right\rangle$
t	dimensionless time
t_{ref}	reference time, $\left(L_3^2/\alpha\right) Ra^{-1/2}$
T	temperature
ΔT	temperature difference, $(T_H - T_C)$
$\mathbf{u}$	dimensionless velocity vector field, $\mathbf{u} = (u_1, u_2, u_3)$
u_{ref}	reference velocity, $(\alpha/L_3)\, Ra^{1/2}$
(x_1, x_2, x_3)	dimensionless spatial coordinates
x_3^{Tr}	x_3-position of $\sigma\,(Nu)_{max}$ on the vertical hot wall

Greek symbols

α	thermal diffusivity
β	thermal expansion coefficient
γ_i	mesh concentration parameters
Δt	time step
Δx_i	mesh size in x_i-directions
ϵ	filter length
θ	dimensionless temperature, $(T-(T_H+T_C)/2)/(T_H-T_C)$
θ_{avg}^{top}	dimensionless averaged temperature at the top wall
μ_{Nu}	first moment of $Nu(x_3)$ about $x_3=0.5$, $\int_0^1(0.5-x_3)Nu(x_3)dx_3$
ν	kinematic viscosity
ρ	fluid density
$\sigma(\cdot)$	standard deviation
$\boldsymbol{\omega}$	vorticity, $\nabla\times\mathbf{u}$
$\mathbf{\Omega}$	diagonal matrix with sizes of control volumes

Subscripts

C	cold wall
f	index for faces of control volumes
h	discrete scalar or vector field
H	hot wall
max	maximum value
min	minimum value
ref	reference quantity

Superscripts

$(\cdot)'$	fluctuations around the mean value
$\langle\cdot\rangle$	time-averaged
$\hat{(\cdot)}_k$	Fourier coefficient at wavenumber k
$\overline{(\cdot)}$	linear filter
$(\cdot)^*$	complex conjugate

1. Introduction

Natural convection in differentially heated cavities (DHC) has been the subject of numerous studies over the past decades. They model many engineering

applications such as ventilation of rooms, cooling of electronic devices or air flow in buildings. Simultaneously, since the pioneering works by Vahl Davis [1] and Ghia *et al.* [2], flows in enclosed cavities has served as prototype for the development of numerical algorithms (examples of thereof can be found in [3, 4, 5, 6], for instance). A schema of the DHC problem is displayed in Figure 1 (left). An accurate prediction of the flow structure and the heat transfer in such a configuration is of great interest and despite the great effort devoted (see for instance [7, 8, 9, 10, 11, 12]) for an accurate turbulence modeling of this configuration it remains a great challenge. This is mainly due to the complex behavior exhibit (see Figure 1, right): the boundary layers remain laminar in their upstream part up to the point where the waves traveling downstream grow up enough to disrupt the boundary layers ejecting large unsteady eddies. The mixing effect of these eddies results in almost isothermal hot upper and cold lower regions, and forces the temperature drop in the core of the cavity to occur in a smaller region. Therefore, an accurate prediction of the transition point is crucial to determine correctly the flow structure in the cavity. However, the high sensitivity of the thermal boundary layer to external disturbances makes it difficult to predict. In conclusion, the DHC is a challenging configuration for turbulence modeling since areas with completely different regimes coexist and interplay.

1.1. DNS and regularization modeling of turbulence

Here, the adopted configuration corresponds to an air-filled ($Pr = 0.7$) cavity of height aspect ratio $A_3 = 5$ at Rayleigh number $Ra = 4.5 \times 10^{10}$ (based on the cavity height, L_3). This resembles the pioneering experimental set-up performed by Cheesewright *et al.* [13] in the mid-80s. Since then, their results have been widely used for benchmarking purposes to validate turbulence models (see [14, 15, 16, 17, 18, 19, 11, 12], for instance); therefore, the availability of accurate numerical results is of extreme importance. To that end, a new complete direct numerical simulation (DNS) has been performed. To do so, the incompressible Navier-Stokes (NS) equations have been discretized preserving the (skew)symmetries of the underlying continuous differential operators [20]. In this way, certain fundamental properties such as the inviscid invariants - kinetic energy, enstrophy (in 2D) and helicity (in 3D) - are exactly preserved in

a discrete sense. However, DNS at high Ra numbers is not feasible. Therefore, a dynamically less complex mathematical formulation is needed.

In the quest for such a formulation, we consider regularizations [21] (smooth approximations) of the convective term that preserve the symmetry and conservation properties exactly. This requirement yielded a novel class of regularizations [22] that restrain the convective production of smaller and smaller scales of motion in an unconditionally stable manner. The numerical algorithm used to solve the governing equations preserves the symmetries and conservation properties too [20] and is therefore well-suited to test the proposed simulation model. The regularization makes use of a normalized self-adjoint filter. In the initial tests [22, 23], the performance of the method was tested keeping the ratio filter length/grid width constant. Thus, this parameter had to be prescribed in advance and therefore a convergence analysis was needed. Later, to circumvent this, a parameter-free approach was proposed [24]. To do so, we proposed to determine the regularization parameter (the local filter length) dynamically from the requirement that the vortex-stretching must be stopped at the scale set by the grid. However, in this way, some of the basic properties of the filter (*i.e.*, symmetry, normalization, incompressibility ...) are lost. Therefore, they need to be restored by explicitly forcing them. However, such *a posteriori* modifications are artifacts that may change the dynamics of the system. To minimize such effects, a new family of discrete linear filters that preserve such list of properties by construction has been recently proposed in [25]. They are based on polynomial functions of the discrete Laplacian operator. In this way, a list of properties is automatically satisfied *per se*: (i) the filter is exactly symmetric and normalized, (ii) the diffusive nature of the filter implies that it does not introduce any non-physical transport between scales and (iii) a filtered divergence-free vector remains 'almost' incompressible. Then, the exact coefficients follow from the requirement that the damping of all triadic interactions at the smallest scale must become virtually independent of the interacting pairs. The latter is a crucial property to control the subtle balance between convection and diffusion. Here, the performance of the proposed method is tested for the aforementioned DHC problem.

The rest of the paper is arranged as follows. In the next section, the test-case is defined and the numerical methods used for the DNS are briefly outlined. Then, most relevant results are presented and discussed. In Section 3, the symmetry-preserving regularization modeling is presented. Discussion is mainly focused on two fundamental issues: (i) the criterion to determine the local filter length and (ii) the construction of suitable discrete linear filters. In Section 4, the performance of the proposed method is evaluated for the aforementioned DHC problem by direct comparison with the DNS data. Finally, relevant results are summarized and conclusions are given.

2. Direct numerical simulation

2.1. Governing equations and numerical methods

The dimensionless incompressible NS equations coupled with the temperature transport equation are considered

$$\partial_t \mathbf{u} + \mathcal{C}\left(\mathbf{u},\mathbf{u}\right) = \mathcal{D}\mathbf{u} - \nabla p + \mathbf{f}, \tag{1}$$

$$\partial_t \theta + \mathcal{C}\left(\mathbf{u},\theta\right) = Pr^{-1}\mathcal{D}\theta, \tag{2}$$

where the convective and diffusive terms are respectively defined by $\mathcal{C}\left(\mathbf{u},\phi\right) = (\mathbf{u}\cdot\nabla)\phi$ and $\mathcal{D}\mathbf{u} = PrRa^{-1/2}\Delta\mathbf{u}$, the body force vector is given by $\mathbf{f} = (0,0,Pr\theta)$ (Boussinesq approximation) and the incompressibility constraint reads $\nabla\cdot\mathbf{u} = 0$. Notice that with the reference quantities, $L_{ref} = L_3$ and $t_{ref} = (L_3^2/\alpha)Ra^{-1/2}$, the vertical buoyant velocity, $Pr^{1/2}$, and the characteristic dimensionless Brunt-Väisälä frequency, N, are independent of the Ra. The geometry of the problem is displayed in Figure 1 (left). The computational domain is $L_1 \times L_2 \times L_3$ in the spanwise and the two wall-normal directions, respectively. The cavity is subjected to a temperature difference $\Delta\theta$ across the vertical isothermal walls ($\theta(x_1,0,x_3) = 0.5$, $\theta(x_1,1/A_3,x_3) = -0.5$) while the top and bottom walls are adiabatic. The no-slip boundary condition is imposed on the velocity at the four closing walls, $x_2 = 0, x_2 = 1/A_3, x_3 = 0, x_3 = 1$. Periodic boundary conditions are applied in the x_1-direction.

The incompressible NS equations (1) are discretized on a staggered Cartesian grid using symmetry-preserving discretizations [20]. Shortly, the temporal

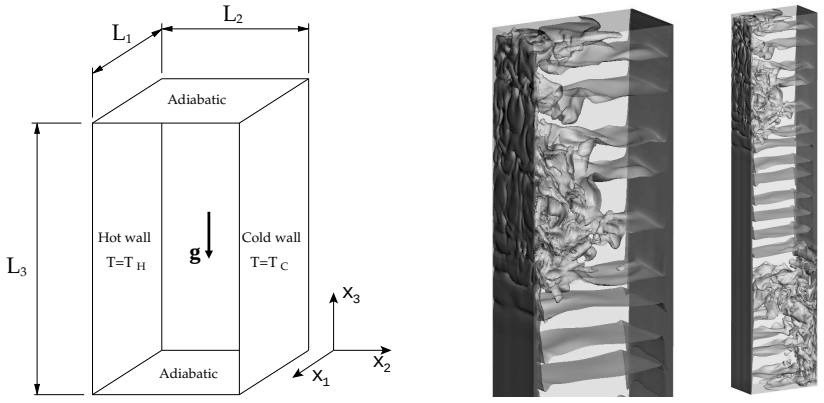

Figure 1: DHC schema (left) and instantaneous isotherms corresponding to the simulation on MeshA (right).

evolution of the spatially discrete staggered velocity vector, $\mathbf{u}_h$, is governed by the following operator-based finite-volume discretization of Eq.(1)

$$\mathbf{\Omega}\frac{d\mathbf{u}_h}{dt} + \mathbf{C}\left(\mathbf{u}_h\right)\mathbf{u}_h + \mathbf{D}\mathbf{u}_h - \mathbf{M}^t\mathbf{p}_h = \mathbf{0}_h, \tag{3}$$

where the discrete incompressibility constraint is given by $\mathbf{M}\mathbf{u}_h = \mathbf{0}_h$. The diffusive matrix, $\mathbf{D}$, is symmetric and positive semi-definite; it represents the integral of the diffusive flux, $-PrRa^{-1/2}\nabla\mathbf{u}\cdot\boldsymbol{n}$, through the faces. The diagonal matrix, $\mathbf{\Omega}$, describes the sizes of the control volumes and the approximate, convective flux is discretized as in [20]. The resulting convective matrix, $\mathbf{C}\left(\mathbf{u}_h\right)$, is skew-symmetric, *i.e.* $\mathbf{C}\left(\mathbf{u}_h\right) = -\mathbf{C}^t\left(\mathbf{u}_h\right)$. Regarding the time evolution of the cell-centered temperature, θ_h , it is discretized in the same way. Then, for the temporal discretization, a second-order explicit one-leg scheme is used for both the convective and diffusive terms. Finally, the pressure-velocity coupling is then solved by means of a classical fractional step projection method [26]: a predictor velocity, $\mathbf{u}_h^p$, is explicitly evaluated without considering the contribution of the pressure gradient. Then, by imposing the incompressibility constraint, $\mathbf{M}\mathbf{u}_h^{n+1} = \mathbf{0}_h$, it leads to a Poisson equation for $\mathbf{p}_h^{n+1}$ to be solved once each time-step,

$$\mathbf{L}\mathbf{p}_h^{n+1} = \mathbf{M}\mathbf{u}_h^p \qquad \text{with} \qquad \mathbf{L} = -\mathbf{M}\mathbf{\Omega}^{-1}\mathbf{M}^t, \tag{4}$$

where the discrete Laplacian operator, $\mathbf{L}$, is represented by a symmetric nega-

tive semi-definite matrix. For details about the numerical algorithms and the verification of the DNS code the reader is referred to [27].

2.2. Verification of the simulation

Results are averaged over the three statistically invariant transformations (time, x_1-direction and central point symmetry). Since no subgrid-scale model is used, the grid resolution and the time step must be fine enough to capture well all the relevant turbulent scales. Moreover, the domain in the periodic direction, L_1, must be long enough, keeping an adequate mesh resolution, Δx_1, to ensure that numerical solution is not affected. Finally, the starting time for averaging and the time integration period must also be long enough to evaluate the flow statistics properly.

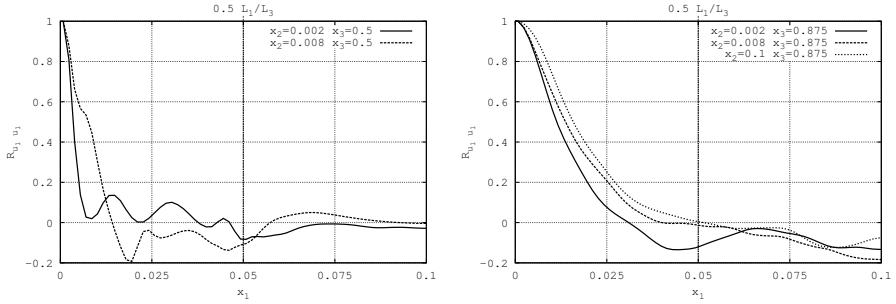

Figure 2: Two-point correlations of the spanwise velocity, u_1, at five monitoring locations.

In a preliminary simulation, we have used a $128 \times 160 \times 432$ (MeshB) Cartesian staggered grid to cover the computational domain (see Table 1 for details). In this case, spatial discretization is second-order accurate [20] and the span-wise length was set to $A_1 = 0.2$. This must be long enough to ensure that turbulence fluctuations are uncorrelated at a separation of one half-period, $A_1/2$. Figure 2 displays spanwise two-point correlation analysis of the spanwise velocity component, $R_{u_1u_1}$, at five different (x_1, x_2)-locations. In all cases, the correlation values fall to zero for separations lower than one half-period. Actually, results show that $A_1 \approx 0.1$ suffices. Similar results are obtained for other (x_1, x_2)-locations and variables. Time-averaged results obtained with MeshB suggested that the transition of the vertical boundary layer may occur at more downstream positions that those observed in the experiments [28] and numerical

Case	N_1	N_2	N_3	A_1	γ_2	γ_3	$(\Delta x_2)_{min}$	$(\Delta x_2)^+_{min}$	Δt	Total time	Average time
MeshA	128	318	862	0.1	2.0	0.0	4.67×10^{-5}	$\lesssim 0.4$	2.85×10^{-4}	420	215
MeshB	128	160	432	0.2	2.0	0.0	9.33×10^{-5}	$\lesssim 0.8$	1.38×10^{-3}	425	180
MeshC	32	80	216	0.1	2.0	0.0	1.87×10^{-4}	$\lesssim 1.6$	4.57×10^{-3}	800	400
RM1	8	20	54	0.1	2.0	1.0	8.93×10^{-4}	$\lesssim 7.6$	3.56×10^{-2}	800	400
RM2	8	14	38	0.1	2.3	1.0	9.25×10^{-4}	$\lesssim 7.9$	5.44×10^{-2}	800	400

Table 1: Physical and numerical simulation parameters.

studies [11, 12]. The accurate prediction of this point is the key ingredient to determine correctly the whole flow configuration in the cavity (for details the reader is referred to [24] and references therein). Then, in order to confirm the results obtained with MeshB, a new DNS simulation with a finer grid $128 \times 318 \times 862$ (MeshA) and $A_1 = 0.1$ has been carried out (see Table 1 for details). In this case, the spatial discretization is fourth-order accurate [20]. Grid spacing in the period x_1-direction is uniform whereas the wall-normal points are distributed using hyperbolic-tangent functions,

$$(x_i)_k = \frac{1}{2}\frac{L_i}{L_3}\left(1 + \frac{tanh\left\{\gamma_i\left(2\left(k-1\right)/N_i - 1\right)\right\}}{tanh\gamma_i}\right), \qquad k = 1, \ldots, N_i + 1. \quad (5)$$

The spatial resolution in these two directions has been determined by means of a systematic procedure based on successive mesh refinements (see [27], for details). The mesh concentration factors, γ_2 and γ_3, are computed to minimize the flow gradients on the computational space for a set of representative instantaneous maps. The region most sensitive to the grid resolution is near the vertical isothermal wall.

In the present simulation (MeshA), the first grid point is located in wall-units at $x_2^+ \lesssim 0.4$ (see Table 1). Note that the friction velocity, u_τ, is computed from the local wall shear stress. Regarding the grid resolution in the periodic direction, it needs to be adjusted to ensure that the smallest scales are well-resolved. To do so, one-dimensional energy spectra at several monitoring points have been used to check the suitability of $\Delta x_1 = A_1/N_1$.

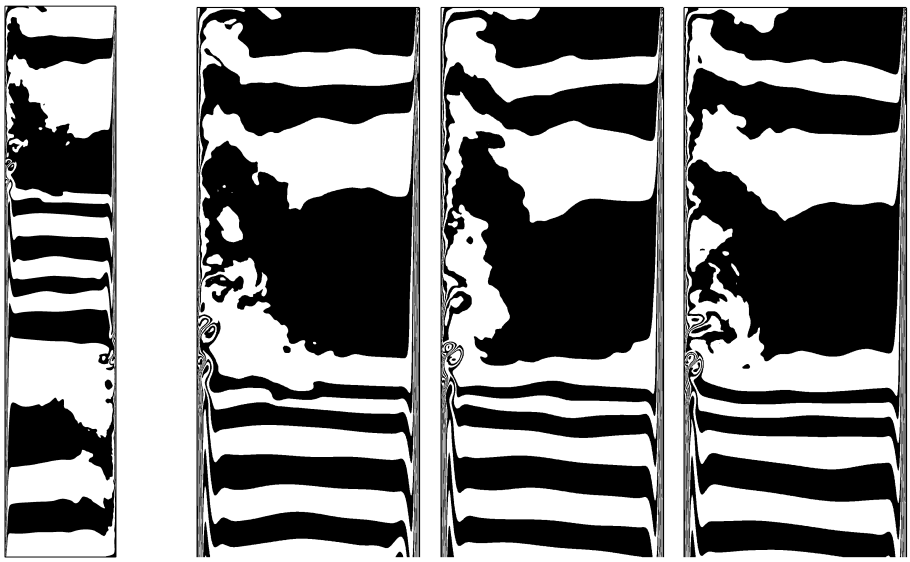

Figure 3: Instantaneous temperature field in a $x_1 = cte$ plane. The isotherms are uniformly distributed from -0.5 to 0.5. Left: general view of the cavity. Right: Time sequence of the top part of the cavity.

2.3. Results and discussion

Instantaneous temperature fields displayed in Figure 3 illustrate the inherent flow complexity of this configuration. Namely, the vertical boundary layers remain laminar in their upstream part up to the point where the waves traveling downstream grow up enough to disrupt the boundary layers ejecting large unsteady eddies. The mixing effect of these eddies results in almost isothermal hot upper and cold lower regions, and forces the temperature drop in the core of the cavity to occur in a smaller region. Turbulent fluctuations are only significant in the downstream part of the boundary layers for x_3-locations downstream the transition point (see Figure 4, right). Therefore, an accurate prediction of the flow structure in the cavity lies on the ability to correctly locate the transition to turbulence. However, the high sensitivity of the thermal boundary layer to external disturbances makes it difficult to predict (see [11], for instance). Regarding this point, significant discrepancies can be found in the literature. The experimental results performed by Cheesewright *et al.* [28] suggested that the transition point in the hot wall occurs around $x_3 \approx 0.2$. However, recent numerical studies [11, 12] are not conclusive at all and their solutions are strongly dependent to meshing parameters and/or the turbulence

model(s) adopted. However, in general, they tend to predict the transition point at much more upstream positions than the one observed for MeshA.

The time-averaged temperature field and the streamlines of the averaged flow together with some turbulent statistics are displayed in Figure 4. These results provide clear evidence of the crucial role of determining the transition point at the vertical boundary layer. Adopting the same criterion than in [27], the transition point, x_3^{Tr}, corresponds to the x_3-position of $\sigma\,(Nu)_{max}$ on the vertical hot wall (see Figure 6). This leads to a value, $x_3^{Tr} \approx 0.674$ for MeshA (0.697 for MeshB), much more downstream than those observed in the above-mentioned experiments and previous numerical studies. Similar discrepancies have also been observed for a turbulent DHC of height aspect ratio 4 when comparing RANS results [12] with DNS results [27]. Also for aspect ratio 4, an experimental study has been recently carried out [29] with Ra up to 1.2×10^{11}. For the highest Ra, the transition point was observed at $x_3^{Tr} \approx 0.3$ (see Figure 11 in [29]) whereas for the DNS at $Ra = 10^{11}$ performed in [30] the transition was observed much more downstream ($x_3^{Tr} \approx 0.61$, see also Figure 1 in [30]). This big gap cannot be attributed to the relatively small difference between Rayleigh numbers. The cause of these discrepancies has not been clarified yet and is currently under investigation. Regarding the experimental set-up performed by Cheesewright *et al.* [13], they may be attributed to the non-Boussinesq effects. It is generally accepted that for air at room temperature the Boussinesq approximation is valid for $\Delta T \lesssim 20K$ [29, 31]. However, the temperature difference in the experimental set-up was significantly higher, namely $\Delta T \approx 46K$ [13]. These effects together with the wall thermal radiation and the heat transfer coupling with the walls should be taken into account for a direct comparison with the experimental results.

Thermal stratification in the core of the cavity is one of the basic questions that has remained opened for several decades. Comparison between numerical and experimental results (see [32] for a detailed review) for a wide range of width/height aspect ratios give completely different results. Experimental studies yield dimensionless stratification of about 0.5 whereas numerical simulations predict values close to 1. Recently, it has been shown that the origin of

such discrepancies is the thermal radiation effects of the front and rear closing walls [33]. In the present work, the thermal stratification is also very close to unity (see Figure 5 and Table 2). Regarding this issue, the prediction of the transition point of the vertical boundary layer also plays a very important role. An example of thereof can be found in [34] where a set of DNS simulations of an air-filled DHC of aspect ratio 4 from weak to fully developed turbulence was presented. Significant changes were observed for the two highest Ra (3×10^{10} and 10^{11}, respectively) for which the transition point at the boundary layers clearly moves upstream. Such displacement increases the top and bottom regions of disorganization shrinking the area in the cavity core where the flow is stratified. Consequently, thermal stratification values significantly greater than unity were measured (1.25 and 1.41, respectively). To give new light to this quest, a new DNS at $Ra = 3 \times 10^{11}$ is currently being performed. For this new case, thermal stratification is ≈ 1.3 and the transition point locates at $x_3^{Tr} \approx 0.55$. Although these are still preliminary results we do not expect significant changes. Hence, again the discrepancies between numerical and experimental data are of the same nature. More importantly, it seems that the thermal stratification tends to reduce after the peak value of 1.41 observed at $Ra = 10^{11}$.

Regarding the heat transfer, the averaged local Nusselt number and its standard deviation for meshes MeshA and MeshB is displayed in Figure 6. Only slight differences are observed around the transition point. As expected, fluctuations are only significant in the downstream part of the boundary layer whereas the upstream remains laminar. The overall Nusselt number obtained with MeshA is 154.5 (155.7 for MeshB). This value is in very good agreement with the value 154.8 predicted by the power-law correlation proposed in [30].

Another important feature of this kind of configuration is the presence of internal waves. Although in the cavity core the averaged velocity (and its fluctuations) are much smaller compared with those observed in the vertical boundary layers, simulations show that in this region isotherms oscillate around the mean horizontal profile. As mentioned-above, the cavity core remains well stratified (see Figures 4 and 3) and, therefore, this phenomenon can be attributed to internal waves. This can be confirmed by analyzing the Nusselt number through

Case	$\langle Nu \rangle$	μ_{Nu}	x_3^{Tr}		C	N
MeshA	154.5	0.156	0.674	0.148	1.002	0.133
MeshB	155.7	0.155	0.697	0.144	1.038	0.136

Table 2: Nusselt number and correlations.

the vertical mid-plane, Nu_c. Time evolution and the normalized density power spectra are displayed in Figures 7 and 8, respectively. The peaks in the spectra are also reported in Table 2 together with the dimensionless Brunt-Väisälä frequency, $N = (CPr)^{0.5}/(2\pi)$, where C is the dimensionless stratification of the time-averaged temperature. Both values are quite similar confirming that internal waves are permanently excited by the eddies ejected form the vertical boundary layer. Hereafter the numerical solution obtained with the MeshA will be referred to as the DNS solution.

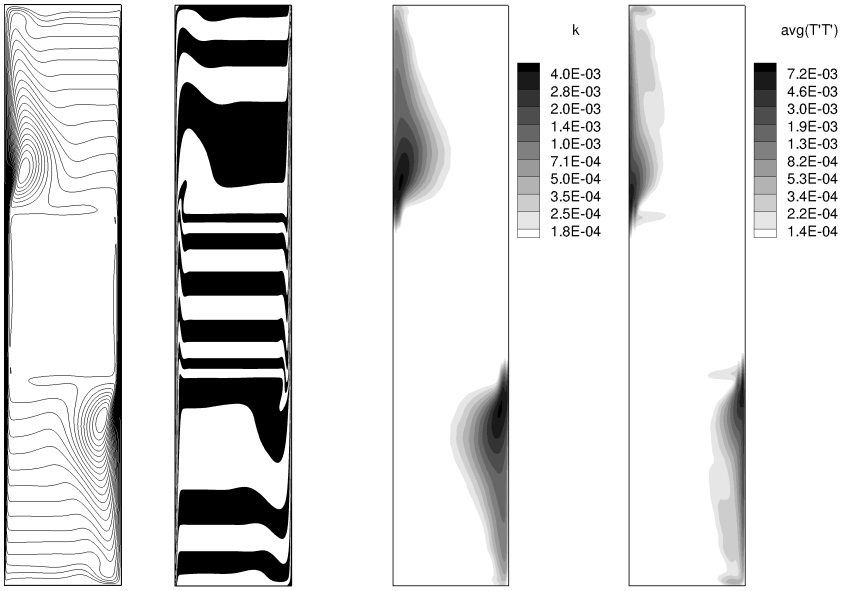

Figure 4: Averaged solutions. From left to right: streamlines, $\langle\theta\rangle$, turbulent kinetic energy and $\langle\theta'\theta'\rangle$. The isotherms are uniformly distributed from -0.5 to 0.5.

3. Turbulence modeling: $\mathcal{C}_4$-regularization

Despite the rapidly growing computing power offered by modern high performance supercomputing systems, direct simulations at high Rayleigh (or Reynolds) numbers are not feasible because the convective term produces far too many

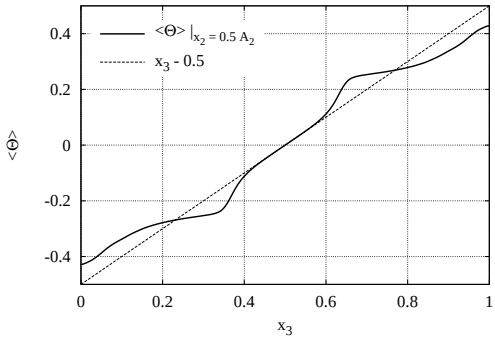

Figure 5: Averaged vertical temperature profile at mid-width.

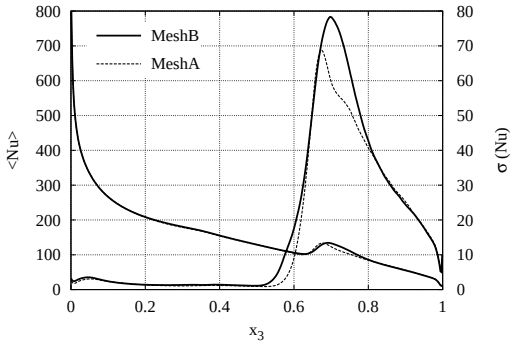

Figure 6: Local Nusselt number distribution and its standard deviation. Comparison between meshes MeshA and MeshB.

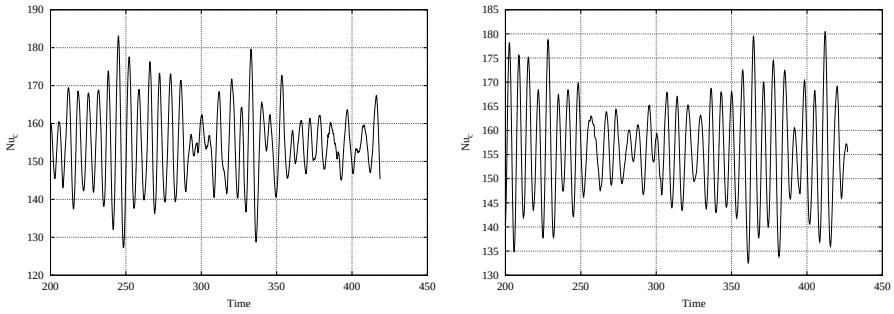

Figure 7: Time evolution of the Nusselt number at the vertical mid-plane for MeshA (left) and MeshB (right).

relevant scales of motion. Therefore, a dynamically less complex mathematical formulation is needed. In the quest for such a formulation, we consider regularizations [35, 21, 36] of the non-linearity. The first outstanding approach in this direction goes back to Leray [37]. The Navier-Stokes-α model also forms an example of regularization modeling (see [21, 38], for instance). The regular-

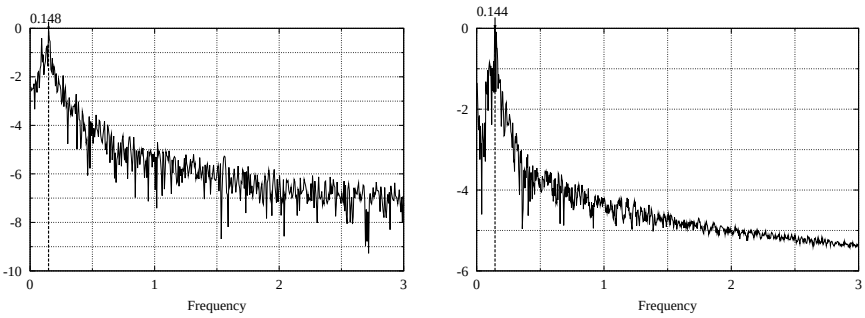

Figure 8: Normalized density power spectra of Nusselt number at the vertical mid-plane for MeshA (left) and MeshB (right).

ization methods basically alter the convective terms to reduce the production of small scales of motion. In doing so, R.Verstappen [22] proposed to preserve exactly the symmetry and conservation properties of the convective terms. This requirement yielded a family of *symmetry-preserving regularization* models: a novel class of regularizations that restrains the convective production of smaller and smaller scales of motion in an unconditionally stable manner, meaning that the velocity cannot blow up in the energy-norm (in 2D also: enstrophy-norm). In our previous works, we restrict ourselves to the $\mathcal{C}_4$ approximation: the convective term in the NS equations (1) is then replaced by the following $\mathcal{O}(\epsilon^4)$-accurate smooth approximation $\mathcal{C}_4(\mathbf{u}, \mathbf{v})$ given by

$$\mathcal{C}_4\left(\mathbf{u}, \mathbf{v}\right) = \mathcal{C}\left(\overline{\mathbf{u}}, \overline{\mathbf{v}}\right) + \overline{\mathcal{C}\left(\overline{\mathbf{u}}, \mathbf{v}'\right)} + \overline{\mathcal{C}\left(\mathbf{u}', \overline{\mathbf{v}}\right)} \tag{6}$$

where the prime indicates the residual of the filter, *e.g.* $\mathbf{u}' = \mathbf{u} - \overline{\mathbf{u}}$, which can be explicitly evaluated, and $\overline{(\cdot)}$ represents a symmetric linear filter with filter length ϵ. Notice that the regularization method is fourth-order accurate respect to ϵ. Hence, it does not affect the order of convergence unless the accuracy of the underlying schemes is higher than four. Moreover, note that the $\mathcal{C}_4$ approximation is also a skew-symmetric operator like the original convective operator. Hence, the same inviscid invariants as for the original NS equations are preserved for the new set of partial differential equations. For further details about the $\mathcal{C}_4$ regularization method the reader is referred to [22, 24].

Regularization makes use of a linear filter. In general, theoretical analysis on regularizations simply assume that the filter is self-adjoint and commutes

with differential operators. Traditionally, in α-type regularizations an inverse Helmholtz operator is used as a filter. Examples of thereof can be found in [39, 40, 22, 41, 42, 43], for instance. However, this is not enough if a regularization wants to be used as a turbulence model. In such a case, we expect it to provide 'very similar' numerical results than those obtained from a DNS but at strongly reduced computational effort. In authors' opinion, the success of regularization modeling basically relies on constructing appropriate filters. To do so, two basic issues need to be carefully addressed. Firstly, a criterion to determine the filter length. This should depend on the local (in space and time) flow conditions and should be able to capture well basic flow features (near-wall behavior, laminar, 2D flows...). Second point refers to discretization of the filter itself. In doing so, a list of basic properties is required for a discrete filter, $\mathbf{F}$. Namely,

(i) Symmetry, $\mathbf{\Omega F} = (\mathbf{\Omega F})^t$.

(ii) Normalization, *i.e.* constant velocity vector is unaffected, $\mathbf{F1}_h = \mathbf{1}_h$.

(iii) Given an incompressible velocity field, $\mathbf{u}_h$ ($\mathbf{M u}_h = \mathbf{0}_h$), $\mathbf{M}\overline{\mathbf{u}}_h = \mathbf{0}_h$.

(iv) Low-pass filtering, *i.e.* only high-frequency components are effectively damped.

(v) The damping effect, $f_4(\widehat{G}_{k_c}, \widehat{G}_p, \widehat{G}_q)$ must be virtually independent of the interacting pair $(p, q = k_c - p)$; that is Eq.(11) need to be satisfied.

The last property is listed here for convenience although the damping function, f_4, has not been introduced yet. Further details about the properties of the linear filter can be found in [25]. These two issues are briefly addressed in the next subsections.

3.1. Stopping the vortex-stretching mechanism

Taking the curl of the NS equations (1) with the convective term replaced by Eq.(6) leads to

$$\partial_t \boldsymbol{\omega} + \mathcal{C}_4\left(\mathbf{u}, \boldsymbol{\omega}\right) = \mathcal{C}_4\left(\boldsymbol{\omega}, \mathbf{u}\right) + \mathcal{D}\boldsymbol{\omega}, \tag{7}$$

where $\boldsymbol{\omega} = \nabla \times \mathbf{u}$ is the vorticity. This equation resembles the vorticity equation that results from the NS equations: the only difference is that $\mathcal{C}$ is replaced by its regularization $\mathcal{C}_4$. If it happens that the vortex-stretching term $\mathcal{C}_4\left(\boldsymbol{\omega}, \mathbf{u}\right)$ in

Eq.(7) is so strong that the dissipative term $\mathcal{D}\boldsymbol{\omega}$ cannot prevent the intensification of vorticity, smaller vortical structures are produced. Left-multiplying the vorticity transport Eq.(7) by $\boldsymbol{\omega}$, we can obtain the evolution of $|\boldsymbol{\omega}|^2$. In this way, the vortex-stretching and dissipation term contributions to $\partial_t|\boldsymbol{\omega}|^2$ result to $\boldsymbol{\omega}\cdot\mathcal{C}_4\left(\boldsymbol{\omega},\mathbf{u}\right)$ and $\boldsymbol{\omega}\cdot\mathcal{D}\boldsymbol{\omega}$, respectively. In order to prevent a local intensification of vorticity, dissipation must dominate the vortex-stretching term contribution at the smallest grid scale, h. In spectral space, this requirement leads to the following inequality

$$\frac{1}{2}\frac{\left(\hat{\boldsymbol{\omega}}_{k_c}\cdot\mathcal{C}_4\left(\boldsymbol{\omega},\mathbf{u}\right)^*_{k_c}+\mathcal{C}_4\left(\boldsymbol{\omega},\mathbf{u}\right)_{k_c}\cdot\hat{\boldsymbol{\omega}}^*_{k_c}\right)}{\hat{\boldsymbol{\omega}}_{k_c}\cdot\hat{\boldsymbol{\omega}}^*_{k_c}}\leq\frac{Pr}{\sqrt{Ra}}k_c^2, \tag{8}$$

where $k_c=\pi/h$ and the vortex-stretching term, $\mathcal{C}_4\left(\boldsymbol{\omega},\mathbf{u}\right)_{k_c}$, is given by

$$\mathcal{C}_4\left(\boldsymbol{\omega},\mathbf{u}\right)_{k_c}=\sum_{p+q=k_c}f_4(\widehat{G}_{k_c},\widehat{G}_p,\widehat{G}_q)\hat{\boldsymbol{\omega}}_p iq\hat{\mathbf{u}}_q, \tag{9}$$

where

$$f_4(\widehat{G}_k,\widehat{G}_p,\widehat{G}_q)=\widehat{G}_k\widehat{G}_p+\widehat{G}_k\widehat{G}_q+\widehat{G}_p\widehat{G}_q-2\widehat{G}_k\widehat{G}_p\widehat{G}_q. \tag{10}$$

Note that $f_4(\widehat{G}_{k_c},\widehat{G}_p,\widehat{G}_q)$ depends on the filter length, ϵ, and in general, on the wavevectors p and $q=k_c-p$. This makes very difficult to control the damping effect because f_4 cannot be taken out of the summation in (9). To avoid this, filters should be constructed from the requirement that the damping effect of all the triadic interactions at the smallest scale must be virtually independent of the interacting pairs, *i.e.*

$$f_4(\widehat{G}_{k_c},\widehat{G}_p,\widehat{G}_q)\approx f_4(\widehat{G}_{k_c}). \tag{11}$$

This is a crucial property to control the subtle balance between convection and diffusion in order to stop the vortex-stretching mechanism. This point was addressed in detail in [25]. The overall damping effect at the smallest grid scale, $f_4(\widehat{G}_{k_c})$, follows straightforwardly

$$f_4(\widehat{G}_{k_c})=\frac{(2Pr/\sqrt{Ra})k_c^2\hat{\boldsymbol{\omega}}_{k_c}\cdot\hat{\boldsymbol{\omega}}^*_{k_c}}{\hat{\boldsymbol{\omega}}_{k_c}\cdot\mathcal{C}\left(\boldsymbol{\omega},\mathbf{u}\right)^*_{k_c}+\mathcal{C}\left(\boldsymbol{\omega},\mathbf{u}\right)_{k_c}\cdot\hat{\boldsymbol{\omega}}^*_{k_c}}, \tag{12}$$

with the condition that $0 < f_4(\widehat{G}_{k_c}) \leq 1$ provided that Eq.(11) is satisfied.

However, the method needs to be applied on a physical domain in $\mathbb{R}^3$. To that end, a novel approach has been recently proposed in [44]. Shortly, the overall damping effect, $f_4(\widehat{G}_{k_c})$ is expressed as a function of the invariants of the local strain tensor, $S(\mathbf{u}) = 1/2(\nabla\mathbf{u} + \nabla\mathbf{u}^t)$. Recalling that the velocity field, $\mathbf{u}$, is solenoidal ($\nabla \cdot \mathbf{u} = 0$); $tr(S) = 0$ and the characteristic equation of S reads

$$\lambda^3 + Q\lambda + R = 0, \tag{13}$$

where $R = -1/3tr(S^3) = -det(S) = -\lambda_1\lambda_2\lambda_3$ and $Q = -1/2tr(S^2) = -1/2(\lambda_1^2 + \lambda_2^2 + \lambda_3^2)$ are the invariants of S, respectively. We order the eigenvalues of S by $\lambda_1 \leq \lambda_2 \leq \lambda_3$. Let us now consider an arbitrary part of the flow domain Ω with periodic boundary conditions. The inner-product is defined in the usual way: $(a, b) = \int_\Omega a \cdot b d\Omega$. Then, taking the L^2 inner-product of (1) with $-\Delta\mathbf{u}$ leads to the enstrophy equation

$$\frac{1}{2}\frac{d}{dt}|\boldsymbol{\omega}|^2 = (\boldsymbol{\omega}, \mathcal{C}(\boldsymbol{\omega}, \mathbf{u})) - \frac{Pr}{\sqrt{Ra}}(\nabla\boldsymbol{\omega}, \nabla\boldsymbol{\omega}), \tag{14}$$

where $|\boldsymbol{\omega}|^2 = (\boldsymbol{\omega}, \boldsymbol{\omega})$. Using the results obtained by [45] and following the same arguments than in [46], it can be shown that the vortex-stretching term can be expressed in terms of the invariant R of $S(\mathbf{u})$

$$(\boldsymbol{\omega}, \mathcal{C}(\boldsymbol{\omega}, \mathbf{u})) = \int_\Omega \boldsymbol{\omega} \cdot S\boldsymbol{\omega} = -\frac{4}{3}\int_\Omega tr(S^3) d\Omega = 4\int_\Omega R d\Omega, \tag{15}$$

and the $L^2(\Omega)$-norm of $\boldsymbol{\omega}$ in terms of the invariant Q

$$|\boldsymbol{\omega}|^2 = -4\int_\Omega Q d\Omega. \tag{16}$$

Then, the diffusive term can be bounded by

$$(\nabla\boldsymbol{\omega}, \nabla\boldsymbol{\omega}) = -(\boldsymbol{\omega}, \Delta\boldsymbol{\omega}) \leq -\lambda_\Delta(\boldsymbol{\omega}, \boldsymbol{\omega}), \tag{17}$$

where $\lambda_\Delta < 0$ is the largest (smallest in absolute value) non-zero eigenvalue of the Laplacian operator Δ on Ω. If we now consider that the domain Ω is

a periodic box of volume h, then $\lambda_\Delta = -(\pi/h)^2$. In a numerical simulation h would be related with the local grid size. Then, to prevent a local intensification of vorticity, *i.e.* $|\boldsymbol{\omega}|_t \leq 0$, the following inequality must be hold

$$f_4(\widehat{G}_{k_c})\frac{(\boldsymbol{\omega}, S\boldsymbol{\omega})}{(\boldsymbol{\omega}, \boldsymbol{\omega})} \leq -\frac{\lambda_\Delta Pr}{\sqrt{Ra}}, \tag{18}$$

where, in this case, $k_c = \pi/h$. This inequality is the analog to Eq.(12) in physical space. Additionally, the dynamics of large scales should not be significantly affected by the (small) scales contained within the domain Ω. This may happen when energy is transferred back to large scales, *i.e.* $(\boldsymbol{\omega}, S\boldsymbol{\omega}) < 0$. Hence, to confine the dynamics of small scales suffices to modify inequality (18) by simply taking the absolute value of its left-hand-side. Then, from Eqs. (15)-(18) and recalling that $0 < f_4 \leq 1$ a proper definition of the overall damping factor at the smallest grid scale follows

$$f_4(\widehat{G}_{k_c}) = \min\left\{\frac{\lambda_\Delta Pr}{\sqrt{Ra}}\frac{Q}{|R|}, 1\right\}. \tag{19}$$

3.2. Numerical methods

The regularization $\mathcal{C}_4$ is constructed in a way that the symmetry properties of the convective operator are exactly preserved [22]. Of course, the same should hold for the numerical approximations that are used to discretize them. For this, the basic ingredients are twofold: (i) a symmetry-preserving discretization of the original NS equations and (ii) a normalized self-adjoint linear filter. The first issue has already been addressed in Section 2.1 where numerical methods for DNS were presented. Actually, both spatial and temporal discretizations are exactly the same than those used for DNS. The second issue is more cumbersome. This point has been recently addressed in [25] where a new family of discrete linear filters was proposed. To sketch the idea behind, linear filters are based on polynomial functions of the discrete diffusive operator,

$$\mathbf{F} = \mathbf{I} + \sum_{m=1}^{\mathcal{M}} d_m \tilde{\mathbf{D}}^m \qquad \text{with} \qquad \tilde{\mathbf{D}} = -(Pr^{-1}Ra^{1/2})\boldsymbol{\Omega}^{-1}\mathbf{D}, \tag{20}$$

where the boundary conditions that supplement the NS equations (1) are applied in (20) too. Notice that the factor $Pr^{-1}Ra^{1/2}$ cancels out the diffusive

constant inside the operator $\mathbf{D}$ defined in Eq.(3). Here we restrict ourselves to the case with $\mathcal{M} = 2$ because it offers a good compromise between accuracy and computational cost. No significant difference has been observed respect to the case with $\mathcal{M} = 3$ whereas the results obtained with $\mathcal{M} = 1$ are significantly worse. Respect to the version originally proposed in [25], an additional restriction needs to be imposed; namely, the coefficient d_2, must be a semi-definite function. This follows from the requirement imposed by filtering in the physical space: in contrast with the spectral approach given by (12), the damping factor at the smallest grid scale, $f_4(\widehat{G}_{k_c})$, and therefore, the set of coefficients $\{d_1, d_2\}$ will also depend on the spatial position. Following the same notation than in [25], the resulting expression for the filter with $\mathcal{M} = 2$ is given by

$$\begin{aligned} d_1 &= -\frac{\widehat{G}_{k_c} - 1}{2\left(2\widehat{G}_{k_c} + 1\right)} \qquad d_2 = \frac{2\widehat{G}_{k_c}^2 - 3\widehat{G}_{k_c} + 1}{16\left(2\widehat{G}_{k_c} + 1\right)} \qquad \text{if} \quad 0 \leq \widehat{G}_{k_c} < 1/2, \\ d_1 &= \frac{1}{4} - \frac{\widehat{G}_{k_c}}{4} \qquad\qquad d_2 = 0 \qquad\qquad\qquad\quad \text{if} \quad 1/2 \leq \widehat{G}_{k_c} \leq 1, \end{aligned} \tag{21}$$

where $\widehat{G}_{k_c}$ is the value of transfer function at the smallest grid scale. The family of filters proposed in (20) is suitable for general multi-dimensional problems. In such a case, the discrete diffusive operator for a cell-centered scalar field, ϕ_h, reads

$$\tilde{\mathbf{D}} = -(Pr^{-1}Ra^{1/2})\mathbf{\Omega}_c^{-1}\mathbf{D} \qquad \text{with} \qquad \mathbf{D} = (PrRa^{-1/2})\mathbf{M}\mathbf{\Omega}_s^{-1}\mathbf{M}^t, \tag{22}$$

where the subindices c and s are used here to distinguish between cell-centered and staggered operators. It must be noted that the diffusive matrix, $\mathbf{D}$, is by construction, symmetric and positive definite and its action on an arbitrary centered cell k of volume $(\mathbf{\Omega}_c)_{k,k}$ is given by

$$[\mathbf{D}\phi_h]_k = \frac{Pr}{\sqrt{Ra}} \sum_{f \in F_f(k)} \frac{(\phi_{c2} - \phi_{c1})\, A_f}{\delta n_f}, \tag{23}$$

where $F_f(k)$ is the set of faces bordering the cell k, A_f is the area of the face f, and $c1$ and $c2$ are the cells adjacent to the face f. The length $\delta n_f = \overrightarrow{n_f} \cdot \overrightarrow{c1c2}$, where $\overrightarrow{n_f}$ is the unitary normal vector of face f and $\overrightarrow{c1c2}$ is the vector between centroids of cells $c1$ and $c2$ (see Figure 9, right). Finally, the volume of the

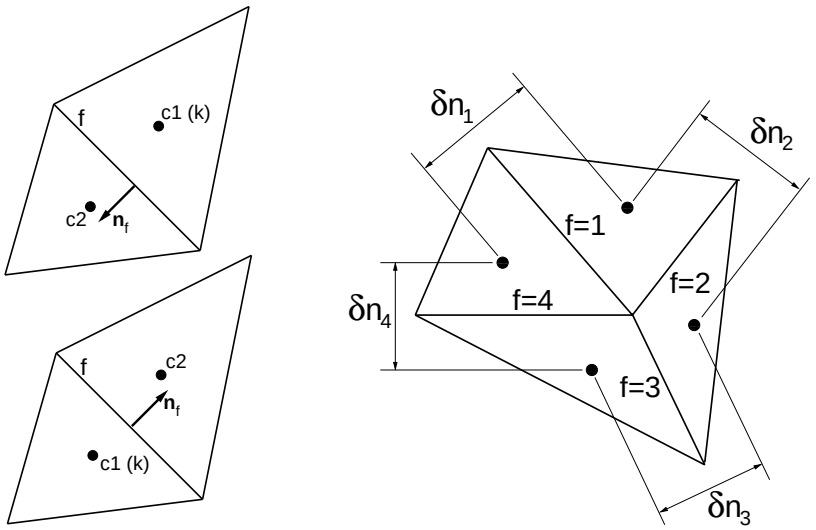

Figure 9: Left: face normal and neighbor labeling criteria. Right: definition of volumes of the face-normal velocity cell.

face-normal cell at the face f, $(\mathbf{\Omega}_s)_f$, is given by $(\mathbf{\Omega}_s)_f = A_f \delta n_f$.

However, since vortex-stretching must be restrained in the whole spatial domain, the set of coefficients $\{d_1, d_2\}$ would follow from the minimum value of f_4. Doing so, we could guarantee that vortex-stretching is effectively stopped; however, the damping effect in some parts of the domain would be indeed excessive. Alternatively, here we propose to construct filters with the general form

$$\mathbf{F} = \mathbf{I} + \sum_{m}^{\mathcal{M}} \left(\tilde{\mathbf{D}}_m\right)^m \quad \text{with} \quad \tilde{\mathbf{D}}_m = -\mathbf{\Omega}_c^{-1}\mathbf{M}\left(\mathbf{\Lambda}_m\right)^{1/m}\mathbf{J}^2\mathbf{\Omega}_s^{-1}\mathbf{M}^t, \tag{24}$$

where $\mathbf{J}$ and $\mathbf{\Lambda}_m$ are diagonal matrices. $\mathbf{J}$ contains the distances between adjacent nodes and $\mathbf{\Lambda}_m$ represents the local coefficients d_m arising given by Eq.(21)

$$[\mathbf{J}]_{f,f} = \delta n_f \qquad \text{and} \qquad [\mathbf{\Lambda}_m]_{f,f} = (d_m)_f. \tag{25}$$

In this way, local values of d_m can be used while keeping all the above-mentioned global properties automatically satisfied. In short, (i) and (ii) follow from the symmetry of $(\mathbf{\Omega}_c\tilde{\mathbf{D}}_m) = (\mathbf{\Omega}_c\tilde{\mathbf{D}}_m)^t$ and the fact that the unity vector lies on the kernel of $\mathbf{M}^t$, *i.e.* $\mathbf{M}^t\mathbf{1}_h = \mathbf{0}_h$. With regard to the property (iii), it is ensured by projecting the filtered velocity field. The latter requires to solve an

additional Poisson equation. The algorithm to determine the discrete filter, $\mathbf{F}$, is summarized in Algorithm 1, whereas the global algorithm to compute the $\mathcal{C}_4$-regularization modeling is outlined in Algorithm 2.

Algorithm 1

1. Compute the invariants Q and R.
2. Determine the local value of $f_4(\widehat{G}_{k_c})$ from Eq.(19) with $(\lambda_\Delta)_f = -(\pi/\delta n_f)^2$.
3. Assuming the the condition (11) is satisfied and recalling that $\widehat{G}_0 = 1$, $\widehat{G}_{k_c}$ follows from Eq. (10): $2\widehat{G}_{k_c} - \widehat{G}_{k_c}^2 \approx f_4(\widehat{G}_{k_c})$.
4. Determine the local values for d_1 and d_2 given by Eq.(21).
5. Construct a symmetric discrete filter, $\mathbf{F}$, from the formula (24) with $\mathcal{M} = 2$.

Algorithm 2

1. Compute the discrete filter, $\mathbf{F}$, following the Algorithm 1.
2. Compute $\overline{\mathbf{u}}_h$ and its residual: $\overline{\mathbf{u}}_h = \mathbf{F}\mathbf{u}_h$ and $\mathbf{u}'_h = \mathbf{u}_h - \overline{\mathbf{u}}_h$.
3. Solve the following Poisson equation: $-\mathbf{M}\boldsymbol{\Omega}_s^{-1}\mathbf{M}^t\mathbf{q}_h = \mathbf{M}\overline{\mathbf{u}}_h$.
4. Compute the projected (divergence-free, $\mathbf{M}\overline{\mathbf{u}}_h^p = \mathbf{0}_h$) velocity field, $\overline{\mathbf{u}}_h^p = \overline{\mathbf{u}}_h + \boldsymbol{\Omega}_s^{-1}\mathbf{M}^t\mathbf{q}_h$ and its residual $(\mathbf{u}_h^p)' = \mathbf{u}_h - \overline{\mathbf{u}}_h^p$.
5. Compute $\mathcal{C}_4$ in a discrete sense:

$$\mathbf{C}_4\left(\mathbf{u}_h, \mathbf{u}_h\right) = \mathbf{C}\left(\overline{\mathbf{u}}_h^p\right)\overline{\mathbf{u}}_h + \mathbf{F}\left(\mathbf{C}\left(\overline{\mathbf{u}}_h^p\right)\mathbf{u}'_h + \mathbf{C}\left((\mathbf{u}_h^p)'\right)\overline{\mathbf{u}}_h\right) \tag{26}$$

The computational cost to determine the discrete filter, $\mathbf{F}$, by the Algorithm 1 is not negligible. The question of whether or not the discrete filter needs to be updated at each time step was addressed in [24]. Direct comparison between results obtained updating at each time-step and results updating up to every temporal unit revealed no significant differences. Hence, in the view of lower costs, the discrete filter, $\mathbf{F}$, is recomputed every 0.5 temporal units. Therefore, the step 1 of the Algorithm 2 becomes computationally inexpensive. This is not the case for the rest of the algorithm. The discrete filter, $\mathbf{F}$, must be applied twice (steps 2 and 5). Since $\mathcal{M} = 2$, the computational cost of filtering is about 3 times the cost of computing the diffusive operator. Moreover, the convective operator must be computed 3 times in the final step 5 instead of only once. However the most time consuming parts are the steps 3 and 4 where $\overline{\mathbf{u}}_h$ is projected onto a divergence-free space and therefore, and additional Poisson equation must be solved (step 3). Finally, two residuals are computed in steps 2 and 5. In practice, compared with the computational cost of a no-

model simulation on the same grid, the $\mathcal{C}_4$ regularization is about twice more expensive.

4. Performance of the $\mathcal{C}_4$-regularization for a turbulent DHC

In the present work, we test the performance of the $\mathcal{C}_4$-regularization method in conjunction with the new family of discrete filters proposed in [25] by means of direct comparison with the DNS results presented in Section 2. We have firstly considered two coarse meshes consisting of $8 \times 14 \times 38$ (RM2) and $8 \times 20 \times 54$ (RM1) grid points, respectively (see Table 1 for details). The meshes are constructed keeping the same grid points distribution as for the DNS but with much coarser spatial resolution. Notice that for the coarsest mesh (RM2) the concentration parameter in the x_2-direction has been slightly modified in order to increase the grid resolution near the vertical walls. The domain size in the periodic direction is the same as for the DNS, *i.e.* $A_1 = 0.1$.

	DNS	RM1		RM2	
Mesh	$128 \times 318 \times 862$	$8 \times 20 \times 54$		$8 \times 14 \times 38$	
		No model	$\mathcal{C}_4$	No model	$\mathcal{C}_4$
Nu	154.5	223.8	**153.4**	207.7	**152.3**
Nu_{max}	781.5	520.6	709.4	500.4	680.0
Nu_{min}	10.5	60.4	7.1	71.0	6.1

Table 3: The overall, the maximum and the minimum of the averaged Nusselt number.

In Table 3, the overall Nusselt number, Nu, together with the maximum and minimum local Nusselt numbers obtained with the coarse meshes RM1 and RM2 are compared with the DNS reference solution computed on MeshA. Regarding the Nu, $\mathcal{C}_4$ solutions are able to provide good predictions whereas the results obtained with the same meshes but without any modeling are very far from the reference value $Nu = 154.5$. With regard to Nu_{max} and Nu_{min}, this tendency becomes even more evident. These two quantities are of interest because they occur in two clearly different parts of the vertical boundary layers. Maximum values occur in the upstream part of the boundary layer where it is still almost laminar whereas minimum values are observed at the most downstream part of the boundary layer where it has become fully turbulent (see

Figure 1, right). Although significant improvements are observed for the regularized solutions the results for the Nu_{max} are not completely satisfactory yet. This is probably due to the insufficient grid resolution that does not allow to properly capture the Nusselt peak in the upstream part of the vertical boundary layer.

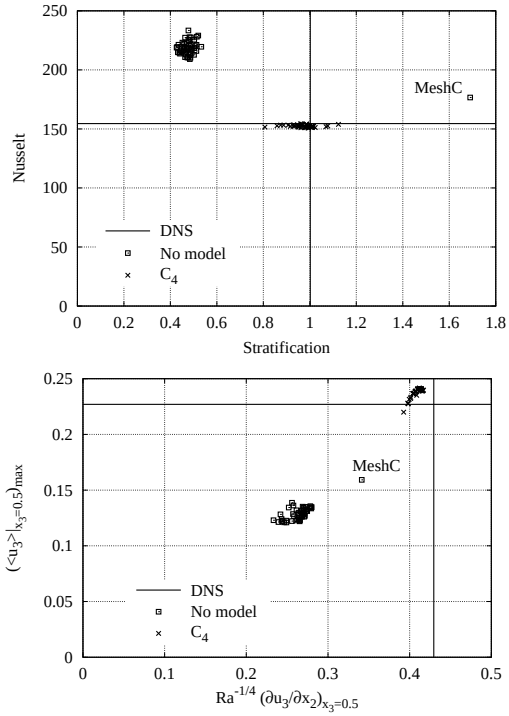

Figure 10: Top: The overall Nusselt number and the centerline stratification. Bottom: The maximum vertical velocity and the wall shear stress scaled by $Ra^{-1/4}$ at the horizontal mid-height plane. Results have been obtained for 50 randomly generated grids. Results obtained with the MeshC are also displayed for comparison.

In order to confirm the reliability of the model on coarse grids, the same DHC problem has been solved on a series of 50 randomly generated meshes where the number of grid points varies within the limits: $8 \leq N_1 \leq 12$, $16 \leq N_2 \leq 28$ and $44 \leq N_3 \leq 70$, respectively. The concentration parameters, γ_2 and γ_3 are the same than those used for the mesh RM1 (see Table 1). The number of grid points in each direction has been randomly generated irrespectively of the number of points in the other two directions; therefore, some of the numerical experiments correspond to highly skewed meshes. Results for the overall Nusselt and the centerline stratification are displayed in Figure 10 (top). The

very good prediction of Nu for all the tested configurations is remarkable; in contrast, the results obtained without modeling substantially differ from the reference solution. Even more important is the fairly good prediction of the stratification. Notice the inaccuracy of the results obtained with the relatively fine MeshC($32 \times 80 \times 216$). Similar behavior is observed in Figure 10 (bottom) where the results for the maximum vertical velocity and the wall shear stress at the horizontal mid-plane, $x_3 = 0.5$, are displayed. These two quantities provide valuable information about whether the boundary layer is correctly captured by the model. The $\mathcal{C}_4$ solutions predict quite well the $(0.430, 0.227)$ reference solution whereas both quantities are clearly under-predicted when the model is switched off. This behavior can also be observed in the averaged vertical velocity profile displayed in Figure 11 (top). For the results obtained without modeling, the vertical boundary layer is too thick, whereas with the $\mathcal{C}_4$ regularization, the solutions obtained with the meshes RM1 and RM2 agree well with the DNS solution. It is noticeable that even for the relatively fine MeshC (see Table 1) results without model are still far from the reference solution. Figure 11 (bottom) depicts essentially the same for the averaged temperature profile.

The local Nusselt number distributions are displayed in Figure 12. Regularized solutions show a very good agreement except for the transition point. In contrast, the solution without model obtained with the mesh RM1 is not even able to capture well the laminar part of the boundary layer. Even more important, the no-model solution computed with the relatively fine MeshC ($32 \times 80 \times 216$) is still far from the DNS reference solution. Notice that in this case the grid resolution in each spatial direction is 'only' twice coarser than the MeshB (see Table 1); however, it does not suffice to capture well the transition point at the vertical boundary layer. The latter is in good agreement with the 'coarse' DNS results obtained by [11] using similar grid resolutions. At this point, it must be recalled that the numerical discretization itself is also a regularization (see Section 2.1). The numerical schemes used to discretize the governing equations are unconditionally stable and the discrete operators are constructed to mimic the underlying differential operators. The energy of the resolved scales of motion is convected in a stable manner, *i.e.* the discrete convective operator transports energy from a resolved scale of motion to other resolved scales without dissi-

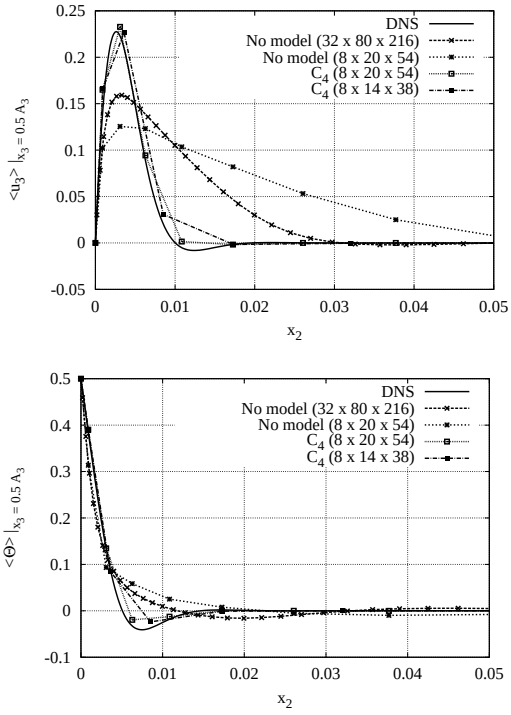

Figure 11: Averaged vertical velocity (top) and temperature (bottom) profiles at the horizontal mid-height plane. Comparison between the DNS, no-model results obtained with MeshC and $\mathcal{C}_4$ results with meshes RM1 and RM2. Details about the meshes can be found in Table 1.

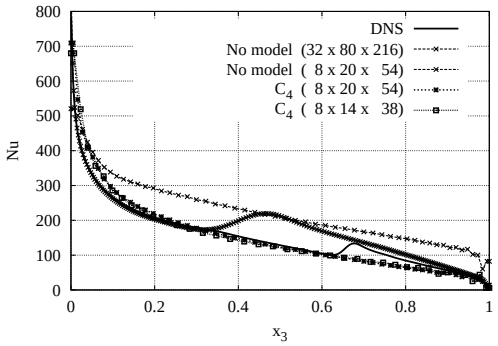

Figure 12: Local Nusselt number distribution. Comparison between the DNS, no-model results obtained with MeshC and $\mathcal{C}_4$ results with meshes RM1 and RM2. Details about the meshes can be found in Table 1.

pating any energy, as it should be from a physical point-of-view. Therefore, their solution ($\epsilon = 0$) constitutes an excellent starting point for any turbulence model. For a detailed explanation, the reader is referred to [20].

Regarding the flow dynamics, the time evolution of the Nusselt number at

the vertical mid-plane together with its normalized density power spectrum are displayed in Figure 13. These results correspond to the coarsest mesh RM2 (for the mesh RM1, the results are almost identical). The results are very similar to those obtained by DNS (see Figures 7 and 8). In this case, the peak in the spectrum is located at slightly lower frequencies. This is probably due to the fact that the stratification is also slightly lower, $C \approx 0.9$. However, it is remarkable that even for the coarsest mesh the model is able to capture well the internal wave motion. Horizontal profiles at the mid-height plane of the turbulent kinetic energy, $k = \langle \mathbf{u}'\mathbf{u}' \rangle$ and the temperature variance, $\langle \theta'\theta' \rangle$, are displayed in Figure 14. An accurate prediction of turbulent quantities at this part of the vertical boundary layer is rather difficult because it is located in an area of transition from the laminar upstream to the turbulent downstream part. At first sight we observe, that although the absolute levels are not always well predicted, the results are in fairly good agreement with the reference solution. Results obtained without model (not displayed here) differ from the DNS solution in several orders of magnitude for both coarse grids. Notice that even for the relatively fine MeshC, the results substantially differ from the reference solution.

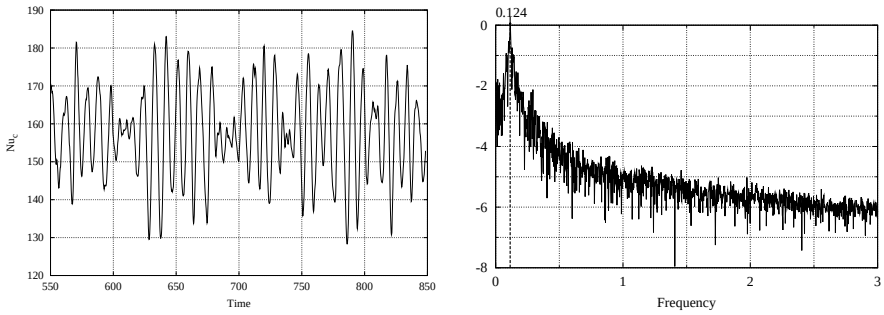

Figure 13: Time evolution of the Nusselt number at the vertical mid-plane for RM2 (left) and its normalized density power spectrum (right).

5. Concluding remarks

A turbulent flow in an air-filled ($Pr = 0.7$) differentially heated cavity at $Ra = 4.5 \times 10^{10}$ and height aspect ratio 5 has been numerically studied. Firstly, a direct simulation has been carried out on a Cartesian staggered mesh with $128 \times 318 \times 862$ grid points. Time-averaged DNS results have revealed that the

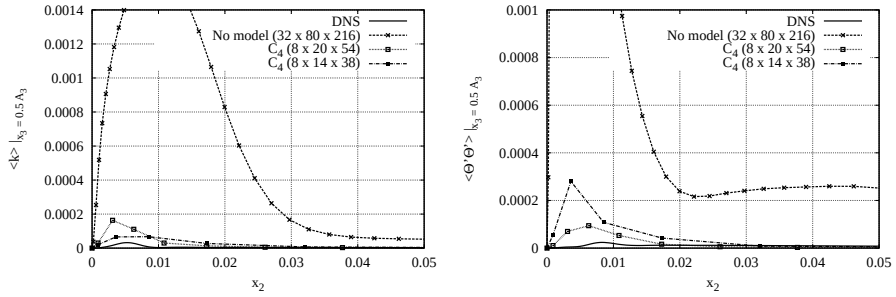

Figure 14: Turbulent kinetic energy $k = \langle \mathbf{u}'\mathbf{u}' \rangle$ (left) and temperature variance $\langle \theta'\theta' \rangle$ (right). Comparison between the DNS, no-model results obtained with MeshC and $\mathcal{C}_4$ results with meshes RM1 and RM2. Details about the meshes can be found in Table 1.

transition of the vertical boundary layer occurs at more downstream positions than those observed in experiments and previous numerical studies. However, since DNS is not feasible for real-world applications the $\mathcal{C}_4$-regularization of the nonlinear convective term has been considered as a simulation shortcut. The symmetries and conservation properties of the original convective term are exactly preserved. Doing so, the production of smaller and smaller scales of motion is restrained in an unconditionally stable manner. The numerical algorithm to solve the governing equations is also fully-conservative and is therefore well-suited to test the proposed simulation method. Here, the performance of the proposed method has been tested for the aforementioned DHC problem. This is a challenging configuration for turbulence modeling since areas with completely different regimes coexist and interplay. Direct comparison with DNS reference results has shown that the method is able to capture the general pattern of the flow correctly even for very coarse meshes. Therefore, considering the inherent difficulty of this problem, we can conclude that the results displayed here illustrate the great potential of the $\mathcal{C}_4$ smoothing method as a simulation shortcut. Moreover, since no *ad hoc* phenomenological arguments that cannot be formally derived from the governing NS equations are used, it suggests that this method may be valid for any other configurations. Nevertheless, more simulations for a wide variety of cases and meshes will be necessary to confirm these preliminary conclusions.

Acknowledgments

This work has been financially supported by the *Ministerio de Ciencia e Innovación*, Spain (ENE2010-17801) and a *Juan de la Cierva* postdoctoral contract (JCI-2009-04910). Calculations have been performed on the IBM MareNostrum supercomputer at the Barcelona Supercomputing Center. The authors thankfully acknowledge these institutions.

References

[1] G. De Vahl Davis. Natural convection of air in a square cavity: A bench mark numerical solution. *International Journal for Numerical Methods in Fluids*, 3:249–264, 1983.

[2] U. Ghia, K. N. Ghia, and C. T. Shin. High-Re solutions for incompressible flow using the Navier-Stokes equations and a multigrid method. *Journal of Computational Physics*, 48(3):387–411, 1982.

[3] W. W. Kim and S. Menon. An unsteady incompressible Navier-Stokes solver for large eddy simulation of turbulent flows. *International Journal for Numerical Methods in Fluids*, 31(6):983–1017, 1999.

[4] L. Agrawal, J. C. Mandal, and A. G. Marathe. Computations of laminar and turbulent mixed convection in a driven cavity using pseudo-compressibility approach. *Computers & Fluids*, 30(5):607–620, 2001.

[5] E. Ertuk and C. Gökçöl. Fourth-order compact formulation of Navier-Stokes equations and driven cavity flow at high Reynolds numbers. *International Journal for Numerical Methods in Fluids*, 50(4):421–436, 2006.

[6] E.D. Dos Santos, G. L. Piccoli, F. H. R. França, and A. P. Petry. Analysis of mixed convection in transient laminar and turbulent flows in driven cavities. *International Journal of Heat and Mass Transfer*, 54(21-22):4585–4595, 2011.

[7] R. A. W. M. Henkes. *Natural-Convection Boundary Layers*. PhD thesis, Faculty of Applied Physics at the Delft University of Technology, 1995.

[8] A. Sergent, P. Joubert, and P. Le Quéré. Development of a local subgrid diffusivity model for large-eddy simulation of buoyancy-driven flows: application to a square differentially heated cavity. *Numerical Heat Transfer, part A*, 44(8):789–810, 2003.

[9] K. J. Hsieh and F. S. Lien. Numerical modeling of buoyancy-driven turbulent flows in enclosures. *International Journal of Heat and Fluid Flow*, 25:659–670, 2004.

[10] S. Kenjereš, S. B. Gunarjo, and K. Hanjalić. Contribution to elliptic relaxation modelling of turbulent natural and mixed ceonvection. *International Journal of Heat and Fluid Flow*, 26:569–586, 2005.

[11] D. G. Barhaghi and L. Davidson. Natural convection boundary layer in a 5:1 cavity. *Physics of Fluids*, 19(12):125106, 2007.

[12] X. Albets-Chico, A.Oliva, and C.D. Pérez-Segarra. Numerical experiments in turbulent natural convection using two-equation eddy-viscosity models. *Journal of Heat Transfer*, 130(7):072501, 2008.

[13] R. Cheesewright, K.J. King, and S. Ziai. Experimental data for the validation of computer codes for the prediction of two-dimensional buoyant cavity flows. In *ASME, Heat Transfer Division, HTD*, volume 60, pages 75–81, 1986.

[14] N. Z. Ince and B. E. Launder. On the computation of buoyancy-driven turbulent flows in rectangular enclosures. *International Journal of Heat and Fluid Flow*, 10(2):110–117, 1989.

[15] T. J. Heindel, S. Ramadhyani, and F. P. Incropera. Assessment of turbulence models for natural convection in an enclosure. *Numerical Heat Transfer, Part B: Fundamentals*, 26(2):147–172, 1994.

[16] C. D. Pérez-Segarra, A. Oliva, M. Costa, and F. Escanes. Numerical experiments in turbulent natural and mixed convection in internal flows. *International Journal of Numerical Methods for Heat and Fluid Flow*, 5(1):13–32, 1995.

[17] S. Murakami, S. Kato, T. Chikamoto, D. Laurence, and D. Blay. New low-Reynolds-number $k-\epsilon$ model including damping effect due to buoyancy in a stratified flow field. *International Journal of Heat and Mass Transfer*, 39(16):3483 – 3496, 1996.

[18] F. Liu and J. X. Wen. Development and validation of an advanced turbulence model for buoyancy driven flows in enclosures. *International Journal of Heat and Mass Transfer*, 42(21):3967 – 3981, 1999.

[19] S. H. Peng and L. Davidson. Computation of turbulent buoyant flows in enclosures with low-Reynolds-number $k-\omega$ models. *International Journal of Heat and Fluid Flow*, 20(2):172–184, 1999.

[20] R. W. C. P. Verstappen and A. E. P. Veldman. Symmetry-Preserving Discretization of Turbulent Flow. *Journal of Computational Physics*, 187:343–368, 2003.

[21] B. J. Geurts and D. D. Holm. Regularization modeling for large-eddy simulation. *Physics of Fluids*, 15:L13–L16, 2003.

[22] Roel Verstappen. On restraining the production of small scales of motion in a turbulent channel flow. *Computers & Fluids*, 37:887–897, 2008.

[23] F. X. Trias, M. Soria, A. Oliva, and R. W. C. P. Verstappen. Regularization models for the simulation of turbulence in a differentially heated cavity. In *Proceedings of the European Computational Fluid Dynamics Conference (ECCOMAS CFD 2006)*, Egmond aan Zee, The Netherlands, September 2006.

[24] F. X. Trias, R. W. C. P. Verstappen, A. Gorobets, M. Soria, and A. Oliva. Parameter-free symmetry-preserving regularization modeling of a turbulent differentially heated cavity. *Computers & Fluids*, 39:1815–1831, 2010.

[25] F. X. Trias and R. W. C. P. Verstappen. On the construction of discrete filters for symmetry-preserving regularization models. *Computers & Fluids*, 40:139–148, 2011.

[26] A. J. Chorin. Numerical Solution of the Navier-Stokes Equations. *Journal of Computational Physics*, 22:745–762, 1968.

[27] F. X. Trias, M. Soria, A. Oliva, and C. D. Pérez-Segarra. Direct numerical simulations of two- and three-dimensional turbulent natural convection flows in a differentially heated cavity of aspect ratio 4. *Journal of Fluid Mechanics*, 586:259–293, 2007.

[28] D. R. Chenoweth and S. Paolucci. Natural Convection in an Enclosed Vertical Air Layer with Large Horizontal Temperature Differences. *Journal of Fluid Mechanics*, 169:173–210, 1986.

[29] D. Saury, N. Rouger, F. Djanna, and F. Penot. Natural convection in an air-filled cavity: Experimental results at large Rayleigh numbers. *International Communications in Heat and Mass Transfer*, 38:679–687, 2011.

[30] F. X. Trias, A. Gorobets, M. Soria, and A. Oliva. Direct numerical simulation of a differentially heated cavity of aspect ratio 4 with Ra-number up to 10^{11} - Part II: Heat transfer and flow dynamics. *International Journal of Heat and Mass Transfer*, 53:674–683, 2010.

[31] D. D. Gray and A. Giorgini. The validity of the boussinesq approximation for liquids and gases. *International Journal of Heat and Mass Transfer*, 19(5):545–551, 1976.

[32] J. Salat, S. Xin, P. Joubert, A. Sergent, F. Penot, and P. Le Quéré. Experimental and numerical investigation of turbulent natural convection in a large air-filled cavity. *International Journal of Heat and Fluid Flow*, 25:824–832, 2004.

[33] S. Xin, J. Salat, P. Joubert, A. Sergent, F. Penot, and P. Le Quéré. Resolving the stratification discrepancy of turbulent natural convection in differentially heated air-filled cavities. Part III: a full convection-conduction-surface radiation coupling. *International Journal of Heat and Fluid Flow*, (under revision).

[34] F. X. Trias, A. Gorobets, M. Soria, and A. Oliva. Direct numerical simulation of a differentially heated cavity of aspect ratio 4 with Ra-number up to 10^{11} - Part I: Numerical methods and time-averaged flow. *International Journal of Heat and Mass Transfer*, 53:665–673, 2010.

[35] J. L. Guermond, J. T. Oden, and S. Prudhomme. Mathematical perspectives on large eddy simulation models for turbulent flows. *Journal of Mathematical Fluid Mechanics*, 6:194–248, 2004.

[36] J. L. Guermond and S. Prudhomme. On the contruction of suitable solutions to the Navier-Stokes equations and questions regarding the definition of large-eddy simulations. *Physica D*, 207:64–78, 2005.

[37] J. Leray. Sur le movement d'un liquide visqueaux emplissant l'espace. *Acta Mathematica*, 63:193–248, 1934.

[38] J. L. Guermond, J. T. Oden, and S. Prudhomme. An interpretation of the Navier-Stokes-alpha model as a frame-indifferent Leray regularization. *Physica D*, 177:23–30, 2003.

[39] A. Cheskidov, D. D. Holm, E. Olson, and E. S. Titi. On a Leray-α model of turbulence. *Proceedings of the Royal Society A: Mathematical, Physical and Engineering Sciences*, 461(2055):629–649, 2005.

[40] B. J. Geurts and D. D. Holm. Leray and LANS-α modelling of turbulent mixing. *Journal of Turbulence*, 7:1–33, 2006.

[41] E. Lunasin, S. Kurien, and E. S. Titi. Spectral scaling of the Leray-α model for two-dimensional turbulence. *Journal of Physics A: Mathematical and Theoretical*, 41(34), 2008.

[42] M. van Reeuwijk, H. J. J. Jonker, and K. Hanjalić. Leray-α simulations of wall-bounded turbulent flows. *International Journal of Heat and Fluid Flow*, 30(6):1044 – 1053, 2009.

[43] T. Y. Kim, M. Neda, L. G. Rebholz, and E. Fried. A numerical study of the Navier-Stokes-$\alpha\beta$ model. *Computer Methods in Applied Mechanics and Engineering*, 200(41-44):2891–2902, 2011.

[44] F. X. Trias, A. Gorobets, C. D. Pérez-Segarra, and A. Oliva. Numerical simulation of turbulence at lower cost: Regularization modeling. *Computers & Fluids*, (published online).

[45] D. Chae. On the spectral dynamics of the deformation tensor and a new a priori estimates for the 3D Euler equations. *Communications in Mathematical Physics*, 263:789–801, 2005.

[46] R. Verstappen. When does eddy viscosity damp subfilter scales sufficiently? *Journal of Scientific Computing*, 49(1):94–110, 2011.